Zamanov, RK, Stoyanov, KA, Wolter, U, Marchev, D, Tomov, NA, Bode, MF, Nikolov, YM, Marchev, V, Iliev, L and Stateva, IK

 An eccentric wave in the circumstellar disc of the Be/X-ray binary X Persei

http://researchonline.ljmu.ac.uk/id/eprint/18576/

Article

For more information please contact researchonline@ljmu.ac.uk

An eccentric wave in the circumstellar disc
of the Be/X-ray binary X Persei

R. K. Zamanov,[1][*] K. A. Stoyanov[1], U. Wolter[2], D. Marchev[3], N. A. Tomov[1],
M. F. Bode[4,5], Y. M. Nikolov[1], V. Marchev[1], L. Iliev[1], I. K. Stateva[1]

[1] *Institute of Astronomy and National Astronomical Observatory, Bulgarian Academy of Sciences, 72 Tsarigradsko Shose,*
1784 Sofia, Bulgaria
[2] *Hamburger Sternwarte, Universität Hamburg, Gojenbergsweg 112, 21029 Hamburg, Germany*
[3] *Department of Physics and Astronomy, Shumen University, 115 Universitetska Str., 9700 Shumen, Bulgaria*
[4] *Astrophysics Research Institute, Liverpool John Moores University, IC2, 149 Brownlow Hill, Liverpool, L3 5RF, UK*
[5] *Office of the Vice Chancellor, Botswana International University of Science and Technology, Private Bag 16, Palapye, Botswana*

ABSTRACT

We present spectroscopic observations of the Be/X-ray binary X Per obtained during the period December 2017 - January 2020 (MJD 58095 - MJD 58865). In December 2017 the $H\alpha$, $H\beta$, and HeI 6678 emission lines were symmetric with violet-to-red peak ratio $V/R \approx 1$. During the first part of the period (December 2017 - August 2018) the V/R-ratio decreased to 0.5 and the asymmetry developed simultaneously in all three lines. In September 2018, a third component with velocity ≈ 250 km s^{-1} appeared on the red side of the HeI line profile. Later this component emerged in $H\beta$, accompanied by the appearance of a red shoulder in $H\alpha$. Assuming that it is due to an eccentric wave in the circumstellar disc, we find that the eccentric wave appeared first in the innermost part of the disc, it spreads out with outflowing velocity $v_{wave} \approx 1.1 \pm 0.2$ km s^{-1}, and the eccentricity of the eccentric wave is $e_{wave} \approx 0.29 \pm 0.07$. A detailed understanding of the origin of such eccentricities would have applications to a wide range of systems from planetary rings to AGNs.

Key words: Stars: emission-line, Be – stars: winds, outflows – circumstellar matter – X-rays: binaries – stars: individual: X Per

1 INTRODUCTION

The relatively bright variable star X Persei (HD 24534) is the optical counterpart of the X-ray source 4U 0352+309 (Braes & Miley 1972) and is classified in the Be/X-ray sub-class of massive X-ray binary stars (e.g. Negueruela 2007; Reig 2011). It consists of an early type Be star and a slowly spinning neutron star. The X-ray data revealed a neutron star with spin period ≈ 836 s, which exhibits quasi-periodic X-ray flares with a period of ~ 7 years (Nakajima et al. 2019). The pulse period shows episodes of spin-up and spin-down (Acuner et al. 2014) which indicates that the neutron star is close to a torque equilibrium and the long pulse period suggests a strong magnetic field (Yatabe et al. 2018). Delgado-Martí et al. (2001) determined the orbital period $\sim$250 d, orbital eccentricity $e = 0.11$, semi-major axis $a =$ 2.2 a.u and orbital inclination $i = 26^0 - 33^0$.

During the last century, the visual brightness of X Per has varied in the range V= 6.8 to 6.2 mag. Spectrograms of X Per from 1913 to 2020 show X Per to have bright hydrogen lines that are variable in structure, velocity, and intensity (e.g. Cowley et al. 1972; Telting et al. 1998). The primary is a rapidly rotating main sequence Be star which forms an outwardly diffusing gaseous disc. It has projected rotational velocity ≈ 215 km s^{-1} (Lyubimkov et al. 1997), and is classified as O9.5 (Fabregat et al. 1992), B0Ve (Roche et al. 1997), B1Ve (Zamanov et al. 2019).

In recent decades, X Per exhibited two disc-loss episodes (around 1977 and around 1989) when the emission lines and the circumstellar disc were missing (Roche et al. 1997; Clark et al. 2001). The long-term variability of the emission lines and optical brightness indicate variable mass ejections from the donor star into the circumstellar disc (Li et al. 2014).

We present optical spectroscopic observations obtained in the last two years and discuss asymmetries in the circumstellar disc and the appearance of eccentric wave.

---

* E-mail: rkz@astro.bas.bg (RKZ), kstoyanov@astro.bas.bg (KAS)
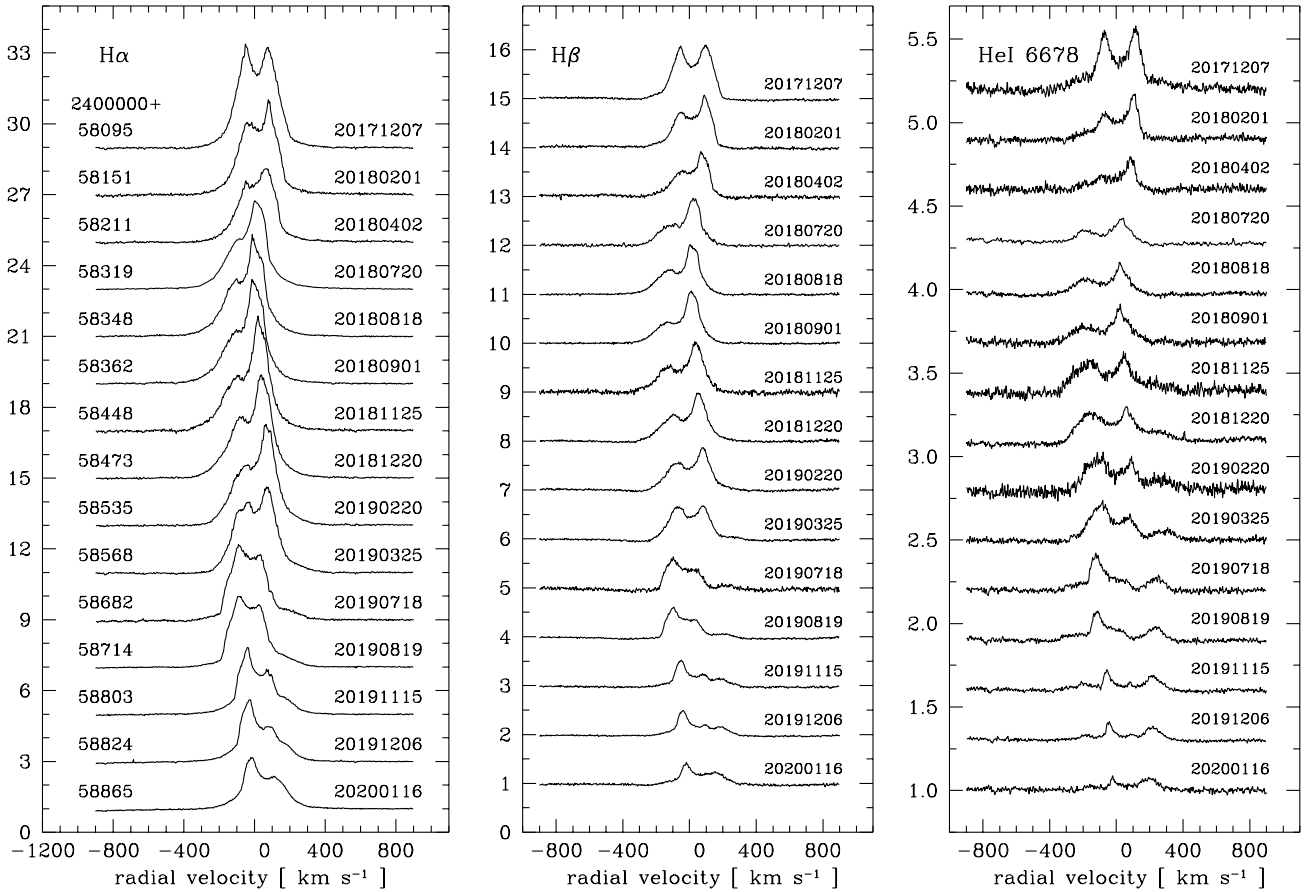
Figure 1. Variability of $H\alpha$, $H\beta$ and HeI 6678 emission line profiles of X Per. The date of observations is in the format YYYYMMDD.

2 OBSERVATIONS

We have 101 optical spectra of X Per on 57 nights secured with the ESpeRo Echelle spectrograph (Bonev et al. 2017) on the 2.0 m RCC telescope of the Rozhen National Astronomical Observatory, Bulgaria and with the HEROS spectrograph (Schmitt et al. 2014) on the 1.2 m TIGRE telescope in the astronomical observatory La Luz in Mexico. The variability of $H\alpha$, $H\beta$ and HeI 6678 emission lines of X Per is presented in Fig. 1. The spectra are normalized to the local continuum and a constant is added to each spectrum. In this figure are plotted only 15 out of 101 spectra obtained.

On the spectra we measure the following parameters: equivalent width of the line, radial velocities of the peaks, intensity of the peaks. To measure the radial velocity we applied Gaussian fitting at the top of the peak. On a few spectra we see three peaks – one violet and two red peaks. In such cases we use the stronger red peak to calculate the distance between the peaks and V/R ratio. The measurements are given in a few tables in the Appendix.

3 RESULTS

During the period December 2017 - January 2020, the equivalent width of the $H\alpha$ emission line ($W\alpha$) varies in the range -26 Å $\leq W\alpha \leq -10$ Å, the equivalent width of the $H\beta$ emission line ($W\beta$) varies in the range -4.4 Å $\leq W\beta \leq -1.4$ Å,

and the equivalent width of the $HeI6678$ emission line varies in the range -2.0 Å $\leq W(HeI6678) \leq -0.4$ Å. The variability of the equivalent widths is presented in Fig. 2, together with V band magnitude and X-ray flux in 2 keV – 10 keV. The V-band data are from the American Association of Variable Star Observers (AAVSO). The X-ray data are from MAXI (Matsuoka et al. 2009). The vertical dashed lines indicate the three periods discussed in Sect. 3.2. There is a correlation between equivalent widths of these three lines. The correlation analysis between $W\alpha$ and $W\beta$, $W\alpha - W(HeI6678)$, $W\beta - W(HeI6678)$ gives correlation coefficient ≥ 0.80, significance $p - value < 10^{-15}$, in other words a very strong correlation between the equivalent widths of the three lines.

It can be seen from Fig. 2 that when the W_α decreases the V band brightness of X Per increases. The connection between W_α and V band magnitude might be caused by the mass ejection from the Be star as discussed in Sect. 4.1 by Li et al. (2014). There are no large changes in the X-ray flux. This indicates that the variability of the emission lines during the period December 2017 - January 2020 does not affect the mass accretion rate onto the neutron star.

3.1 Disc size

The variability of the distance between the peaks is presented in Fig. 3. The emission lines form in the disc surrounding the Be star. The discs of the Be stars are Keplerian supported

by the rotation [e.g. Rivinius et al. (2013), Okazaki (2016) and references therein]. For a Keplerian circumstellar disc the peak separation can be regarded as a measure of the outer radius (R_{disc}) of the emitting disc (Huang 1972):

$$R_{disc} = R_1 \frac{(2\,v\,\sin i)^2}{\Delta V^2}, \tag{1}$$

where R_1 is the radius of the primary and $v \sin i$ is its projected rotational velocity. Radii estimation through this method, is a good approximation for symmetric profiles. The projected rotational velocity of the primary is estimated to be $v \sin i = 200$ km s^{-1} (Slettebak 1982), $v \sin i = 215 \pm 10$ km s^{-1} using the HeI $\lambda 4026$ Å absorption line (Lyubimkov et al. 1997) and $v \sin i = 191 \pm 12$ km s^{-1} from the width of the $H\alpha$ emission (Zamanov et al. 2019). For the primary we adopt $R_1 = 10.5\ R_\odot$ and mass $M_1 = 13.5\ M_\odot$ (Zamanov et al. 2019). This gives the Keplerian velocity on the surface of the star $V_{Kepl} = 495$ km s^{-1}. Adopting inclination $i = 30^0$ (Delgado-Martí et al. 2001), and that the star rotates with 0.8 of the critical velocity (e.g. Porter & Rivinius 2003), we estimate $v \sin i \approx 198$ km s^{-1}, which is in agreement with the above values. This agreement also is a clue that there is no considerable deviation between the orbital plane of the binary and the equatorial plane of the Be star. If it exists at all it should be less then 5°.

On the spectrum 20190325 (see Fig. 1), the HeI emission extends upto ≈ 370 km s^{-1} at zero intensity. We note that velocities in the profiles of the emission lines $> 495 \sin i$ km s^{-1}, which is ≈ 250 km s^{-1}, are probably super-Keplerian velocities, and indicate eccentric motion in the disc, where these parts of the emission line are formed (see Sect. 3.3).

In December 2017 the emission lines have double-peaked symmetric profiles (see Fig. 1). For 5 spectra obtained in December 2017 we measure $\Delta V\alpha = 120 \pm 1$ km s^{-1}, $\Delta V\beta = 150 \pm 1$ km s^{-1}, and $\Delta V_{HeI} = 180 \pm 2$ km s^{-1}. Using Eq. 1, these values correspond to disc size $R_{disc}(H\alpha) = 134\ R_\odot$, $R_{disc}(H\beta) = 86\ R_\odot$, and $R_{disc}(HeI6678) = 60\ R_\odot$. During the period of our observations, the average distance between the peaks of the lines is $\Delta V\alpha = 111 \pm 14$ km s^{-1}, $\Delta V\beta = 142 \pm 13$ km s^{-1}, $\Delta V_{HeI} = 213 \pm 52$ km s^{-1}. These values correspond to the following average disc size for different emission lines (calculated using Eq. 1): $R_{disc}(H\alpha) = 156\ R_\odot$, $R_{disc}(H\beta) = 96\ R_\odot$, $R_{disc}(HeI6678) = 43\ R_\odot$. The typical errors are about ± 5 %. For the calculations of the outflowing velocity (Sect. 4.1) we will use $R_{disc}(H\beta) = 86 - 96\ R_\odot$. The average ratios between disc sizes (which is equivalent to the ratio of the peak separations) are: $R_{disc}(H\alpha)/R_{disc}(H\beta) = 1.62$, $R_{disc}(H\alpha)/R_{disc}(HeI6678) = 3.63$.

3.2 V/R ratio and asymmetries in the disc

In Fig.1 it is seen that the emission lines are symmetric in December 2017, with V/R ratio ≈ 1. After that all three lines become asymmetric. Fig. 4 presents the V/R ratio, calculated as $V/R = (I_V - 1)/(I_R - 1)$, where I_V and I_R are the intensity of the blue (violet) and red peak, respectively. The spectra are normalized before the measurements and the continuum level is $\equiv 1.0$.

(1) During the first part of the period (MJD 58095 - MJD 58365) in all three lines the V/R-ratio varies in practically the same manner – it decreased from $V/R \approx 1$ to $V/R \approx 0.5$, with speed $\frac{\Delta(V/R)}{\Delta t} \approx 2 \times 10^{-3}$ d^{-1}. The fact that
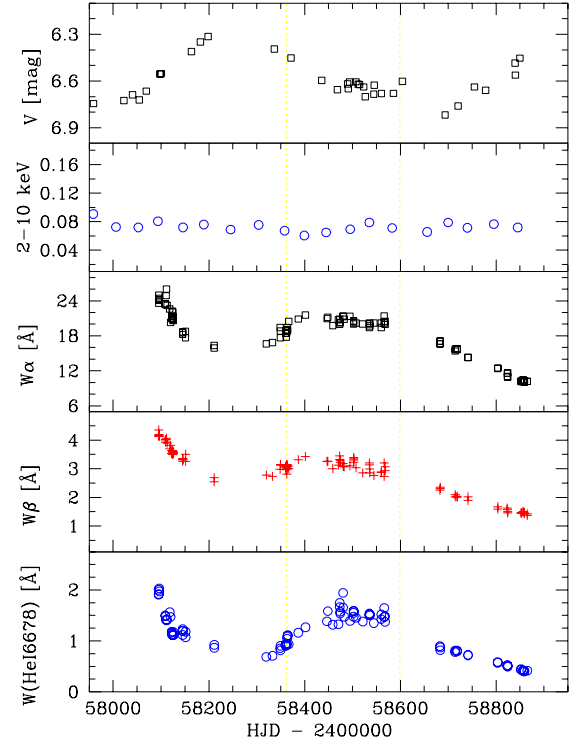
Figure 2. Variability of X Per in V band (AAVSO), 2-10 keV X-rays (MAXI), and the equivalent widths of the emission lines $H\alpha$ (black squares), $H\beta$ (red pluses), and HeI6678 (blue circles).
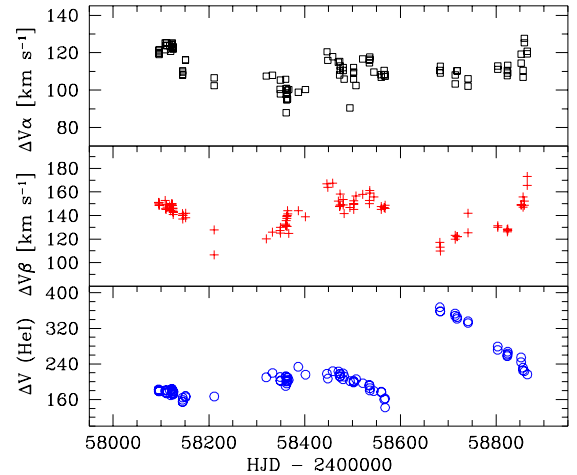
Figure 3. The distance between the peaks of the emission lines – $H\alpha$ (black squares), $H\beta$ (red pluses), and HeI6678 (blue circles).
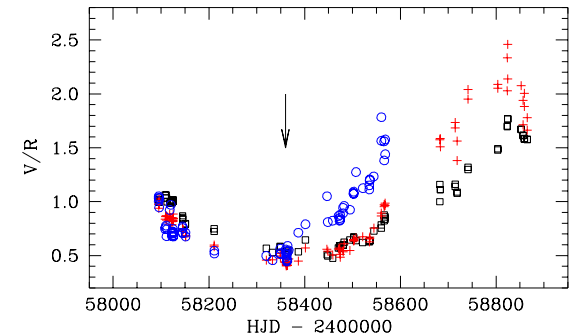
Figure 4. V/R ratio for $H\alpha$ (black squares), $H\beta$ (red pluses), and HeI6678 (blue circles). The arrow indicates the appearance of the eccentric wave.
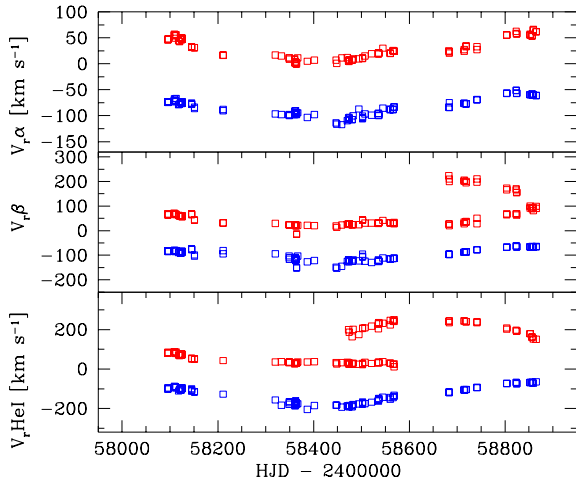
Figure 5. Radial velocities of the peaks.
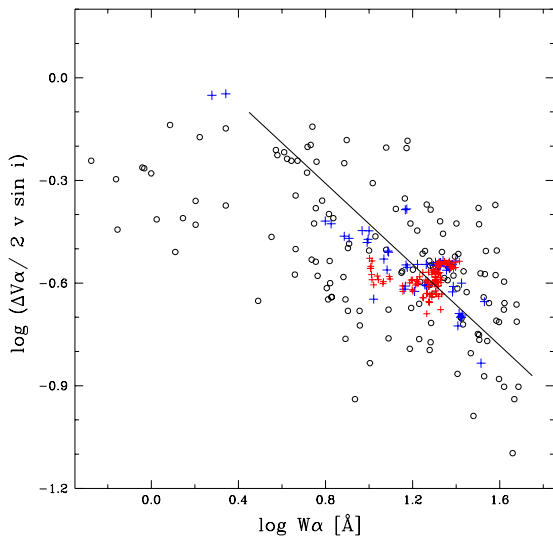
Figure 6. $\Delta V \alpha$ versus W_α. The circles are the Be stars (see text) and the red crosses are our observations of X Per.
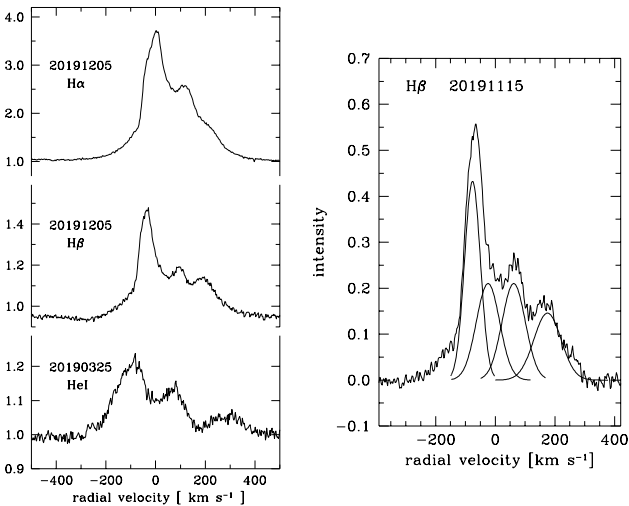
Figure 7. The left panel shows the three component structure of HeI 6678 and $H\beta$ lines, and red shoulder in the $H\alpha$ line. Right panel is an approximation with four Gaussian (see Sect.4.2).

the changes in V/R-ratio are practically identical in all three lines ($H\alpha$, $H\beta$ and HeI, see Fig.4) means that the asymmetry develops in the entire disc simultaneously.

(2) During the second part of the period (MJD58365 - MJD58600) the V/R-ratio of $H\alpha$ and $H\beta$ goes up from 0.5 to ~ 1.0. However the behaviour of the V/R-ratio of HeI6678 deviates from the behaviour of the $H\alpha$ and $H\beta$ lines (see Fig. 4). V/R (HeI) changes from 0.5 to 1.5, having a faster rate of change $\frac{\Delta(V/R)}{\Delta t} \approx 4 \times 10^{-3}$ d^{-1}. For comparison, the $H\alpha$ emission peaks have rate of change $\frac{\Delta(V/R)}{\Delta t} \approx 1.7 \times 10^{-3}$ d^{-1} and the $H\beta$ peaks – $\frac{\Delta(V/R)}{\Delta t} \approx 2.3 \times 10^{-3}$ d^{-1} . In addition to that, a third component appeared in the red side of the HeI profile (Fig. 7). This third component emerged in HeI in November 2018. This is an indication that the structural changes begin in the innermost region of the disc.

(3) The behaviour of the V/R-ratio of $H\beta$ is similar to that of $H\alpha$ till MJD 58600. After it it begins to deviate (see Fig. 4). This is an indication that the asymmetry spreads out in the disc.

The development of asymmetries visible in the $H\alpha$ peaks corresponds to processes in the outer parts, while the variability of HeI is connected with changes in the inner parts of the circumstellar disc.

3.3 Third component in He I

In November 2018 a third component appears in the red side of the HeI line. In March 2019, this component peaks at radial velocity ~ 250 km s^{-1}, and at zero intensity it is in the range 130-390 km s^{-1}. The three component structure is demonstrated on Fig. 7, left panel. The Keplerian velocity around the primary is $V_{Kepl} = \sqrt{GM_1/r}$, where G is the gravitational constant and r is the distance. We estimate that the observed velocity of the third component corresponds to a distance from the centrum of the primary of 40 - 20 $R_\odot$, respectively. Bearing in mind that $R_1 \approx 10.5\ R_\odot$, it means that this component originates somewhere about 1-3 stellar radii above the stellar surface. The velocity of this component is similar to the velocities observed during the double disc formation in 1994 (Tarasov & Roche 1995), when the blue and red peaks of the inner disc were at -308 km s^{-1} and $+258$ km s^{-1}, respectively.

4 ECCENTRIC WAVE

The discs around stars, or other central massive bodies, can support disturbances in which the fluid motion is nearly Keplerian with non-zero eccentricity. The eccentric waves are expected not only in Be discs but also in accretion discs, protoplanetary discs, and in discs with an embedded planet (e.g. Lynch & Ogilvie (2019) and references therein). In X Per, the appearance of a significant density enhancement in the disc near the stellar surface and its evolution was also observed and discussed by Tarasov & Roche (1995) and Clark et al. (2001). Assuming that the observed behaviour of the emission lines of X Per is due to an eccentric wave, we calculate its velocity and eccentricity.

4.1 Velocity of the eccentric wave

We first see the appearance of the third component in HeI lines on our spectrum in November 2018 (20181124). It is not visible on our spectrum obtained in mid-October 2018 (20181010). In March 2019 this component starts to be visible in the red side of $H\beta$. The profile of $H\beta$ on 5 December 2019 (20191205) with three peaks is similar to that of HeI obtained 8 months earlier (20190325), see Fig.7. We suppose that the eccentric wave began somewhere about MJD 58360 (about end of August 2018) when the behaviour of the HeI peaks started to deviate from $H\beta$ and $H\alpha$ (see the arrow on Fig. 4). At this time it is likely to be at a distance $r \geq R_1$. It reached near to the outer edge of the $H\beta$ disc in January 2020 (when the two red peaks of $H\beta$ blended). This indicates that the eccentric wave spreads from inside out. Bearing in mind the disc size in the lines (Sect. 3.1) this corresponds to an outflowing velocity of the wave $v_{wave} \approx 1.2 \pm 0.1$ km s^{-1}.

In the above calculation we supposed that the motion of the density wave is linear. We also supposed that the peak merging corresponds to the moment when the wave reached the outer edge. We performed numerical experiments with Gaussian fitting of the peaks and their blending (merging). The experiments showed that to observe two peaks the difference between their velocities must be $\gtrsim 30$ km s^{-1}. If it is less than 30 km s^{-1} then we will see one peak. This value depends on the signal-to-noise ratio of the spectra, width of the peaks, their intensity, etc. This limit of 30 km s^{-1} was found with numerical experiment with two Gaussian peaks, having width and intensity similar to those observed. This also indicates that the above estimation should be considered as an upper limit of v_{wave}. Assuming that the merging of the peaks corresponds to the moment when the wave is at 0.85 ± 0.15 of the disc size, this will give $v_{wave} \approx 1.1 \pm 0.2$ km s^{-1}.

In Fig. 5 are plotted the heliocentric radial velocities of the peaks for $H\alpha$ ($V_r\alpha$), for $H\beta$ ($V_r\beta$), and for HeI 6678 (V_rHeI). The radial velocities of the HeI peaks indicate that the wave begins somewhere about MJD 58350 (August 2018). The radial velocities of the $H\beta$ peaks indicate that the two red peaks merged somewhere about MJD 58850 (January 2020).

In Fig. 6 we plot distance between the peaks of $H\alpha$ normalized with the stellar rotation versus $W\alpha$. These two parameters correlate in the Be stars, representing the fact that the disc grows as $W\alpha$ increases. The black open circles are data for Be stars taken from Andrillat (1983), Hanuschik (1986), Hanuschik et al. (1988), Dachs et al. (1992), Slettebak et al. (1992), and Catanzaro (2013). The red plus signs are our measurements of X Per. We see that X Per is close to the average behaviour of the Be stars. This indicates that the eccentric wave does not change the overall structure of the circumstellar disc.

4.2 Eccentricity of the eccentric wave

The vis-viva equation, connects the instantaneous orbital speed of a body at any given point in its trajectory with distance. For periastron and apastron we have:

$$v_{per} = \sqrt{GM_1\left(\frac{2}{a(1-e)} - \frac{1}{a}\right)} \tag{2}$$

Table 1. In the table are given date of observations (in the format YYYYMMDD), heliocentric radial velocities of the three peaks, and the calculated eccentricity of the eccentric wave.

date-obs	V_{r1}	V_{r2}	V_{r3}	e_{wave}
HeI 6678				
20190221	-147.2	29.9	231.9	0.17
20190323	-137.7	24.8	247.8	0.23
20190325	-133.4	23.9	246.3	0.24
20190220	-155.1	29.8	249.0	0.18
$H\beta$				
20190819	-89.6	33.0	210.2	0.33
20190822	-86.6	39.2	201.5	0.32
20191115	-67.0	62.0	176.2	0.36
20191206	-65.8	63.6	157.6	0.31
$H\alpha$				
20191115	-57.1	59.8	145.2	0.33
20191115	-56.9	55.0	148.6	0.36
20191206	-63.5	52.3	155.6	0.32

$$v_{ap} = \sqrt{GM_1\left(\frac{2}{a(1+e)} - \frac{1}{a}\right)} \tag{3}$$

where a is the length of the semi-major axis of the elliptical orbit, and $a(1-e)$ and $a(1+e)$ are the distances at which the speed is to be calculated (in our case periastron and apastron, respectively).

Using three spectra on which $H\alpha$ is symmetric (20161211, 20170317, 20171207) we measure the velocity at the half maximum of the $H\alpha$ emission -11 ± 3 km s^{-1}. The measurement is done using the position of the bisector at the half maximum intensity of the emission, as shown in Fig. 1 of Glebocki et al. (1986). The old spectroscopic data of Hutchings (1977) give an average value for the radial velocity of the Balmer absorption ≈ -20 km s^{-1} and for HeI lines -19 ± 10 km s^{-1}. Grundstrom et al. (2007) give systemic velocity $\gamma = 1.0 \pm 0.9$ km s^{-1} on the basis of absorption lines in the IUE spectra. On the spectra where 3 peaks are visible we measure the heliocentric radial velocities of the peaks. They are given in Table 1. For HeI and $H\beta$ these are measurements of the peaks. For $H\alpha$ it is the velocity of the shoulder. Correcting these values for the systemic velocity:
$V_{r1} - \gamma = v_{ap}\sin i$
and
$V_{r3} - \gamma = v_{per}\sin i$,
and using Eq. 2 and Eq. 3, we estimate the eccentricity of the wave, which is given in the last column of Table 1. The average eccentricity of the wave is $e_{wave} = 0.29 \pm 0.07$.

In the above calculations we adopted $\gamma = -11$ km s^{-1}. If we assume $\gamma = -1$ km s^{-1}, the estimated e_{wave} will increase up to $e_{wave} = 0.36 \pm 0.07$. There should be two blue peaks corresponding to the two red peaks. In our spectra we see only one, see Fig. 7 (left panel). It means that the two blue peaks are blended (and have approximately equal velocities). To estimate the possible influence of the blending on our value of e_{wave}, we fitted the profile with four Gaussian (Fig. 7, right

panel). During the fitting we explicitly assumed that the two inner peaks are identical. The fitting suggests that the peak (corresponding to the wave) could be blue shifted with $10 - 20$ km s^{-1}. A correction of -10 km s^{-1} to the measured radial velocity produces a lower value $e_{wave} = 0.24 \pm 0.06$. These two sources of uncertainty give the range $0.16 < e_{wave} < 0.42$ for the eccentricity of the wave.

5   DISCUSSION

Eccentric discs, in which planet, or star, or fluid elements follow elliptical orbits of variable eccentricity around a central mass, have applications in various astrophysical objects: Be stars (Ogilvie 2008), galactic nuclei (Cao et al. 2018), planetary rings and protoplanetary discs (Lee et al. 2019; Martin et al. 2020). A more deep understanding of the appearance and the evolution of asymmetries and eccentricities in the circumstellar disc of X Per and other Be/X-ray binaries would therefore be of general interest. There are different theories about the origin of the long-term variability observed in Be stars [e.g. Hanuschik et al. (1995), Section 4.2]. The most accepted is the global oscillation scenario, which proposes that a Keplerian disc around a Be stars is subject to global distortion – a one-armed density wave (Okazaki 1991; Savonije & Heemskerk 1993; Papaloizou & Savonije 2006), which is an updated and sophisticated version of the old elliptical disc model (Struve 1931). Eccentric mode in Be/X-ray binaries can be excited in the disc through direct driving as a result of a one-armed bar potential of the binary (Okazaki et al. 2002).

In our opinion, during the first part or our observations (MJD 58095 – MJD 58365) we observe a global distortion ($H\alpha$, $H\beta$, HeI vary together) similar to that observed in H $1145 - 619$ (see Fig. 7 by Alfonso-Garzón et al. (2017)). During the period MJD 58365 – MJD 58865, we observe an eccentric wave, which starts in the innermost parts of the disc and spreads out with velocity $v_{wave} \approx 1.1$ km s^{-1}. Once the wave is in the disc, it should begin to rotate. Its rotation is expected to be much slower than the disc rotation (Okazaki & Kato 1986). The radial velocities on Fig. 5 indicate that the period of rotation of the density wave is probably ~ 800 d.

The interesting behavior of the HeI emission of X Per was studied by Kunjaya & Hirata (1995) and by Tarasov & Roche (1995). They observed four peaks in HeI emission in 1995 and suggested the formation of a double circumstellar disc. Hirata & Kogure (1977) were first to argue about the existence of a two component structure of the circumstellar envelope around a Be stars following the example of the well known star Pleione (BU Tau). They proposed a model consisting of two layers and also considered a separate fast rotating layer closer to the stellar equator. The formation of a new envelope, coexisting with the previous one is also detected by Nemravová et al. (2010) on the basis of four peak structure of $H\alpha$ emission. Clark et al. (2001) presented an extensive data set of X Per, covering the period 1987 to 2001, and interpreted the HeI variability as a formation of a density wave which moves towards the outer parts faster than the disc formation. It is likely that the four peaks profiles of X Per in 1995 represented a wave with eccentricity almost zero.

Following Delgado-Martí et al. (2001) the periastron passages of the neutron star is expected at
MJD $51353(\pm 7) + 250.3(\pm 0.6) \times E$.
The excitation of the eccentric wave could be connected with the periastron passage at about MJD 58361. The periastron passage of the neutron star initiates (generates) a higher tidal wave on the stellar surface. Superposition of a high tide with another mechanism (e.g. non-radial pulsations) could cause a mass ejection event from the star surface into the inner disc. A similar mass ejection was already discussed by Li et al. (2014) in connection between the long term variability of the $H\alpha$ line and the X-ray emission from the neutron star. The recent radiative transfer calculations on the structure of Be discs in coplanar circular binary systems suggest a V/R cycle every half orbital period (Panoglou et al. 2018). We do not see signs of such modulation in X Per in our data, which covers 770 days, i.e. more than three orbital periods.

CONCLUSIONS

We report 100 spectral observations of the Be/X-ray binary X Per during the period December 2017 - January 2020. We study the evolution of the profiles of the emission lines $H\alpha$, $H\beta$, and $HeI6678$, which are formed in the Be circumstellar disc. Their evolution suggests an eccentric wave in the circumstellar disc, for which we find that: (1) it spreads from inside out; (2) its velocity is $v_{wave} = 1.1 \pm 0.2$ km s^{-1}; (3) the eccentricity of the eccentric wave is in the range $0.17 \leq e_{wave} \leq 0.41$.

The development of asymmetries in the inner and outer parts of the circumstellar disc in the Be/X-ray binary X Per provides a laboratory to test the theoretical models of eccentric waves in the Be discs. We encourage high-resolution spectroscopic observations of this relatively bright object (e.g. Echelle spectrographs on 2.0m class telescopes) to monitor the evolution of the emission lines.

REFERENCES

Acuner Z., İnam S. Ç., Şahiner Ş., Serim M. M., Baykal A., Swank J., 2014, MNRAS, 444, 457
Alfonso-Garzón J., et al., 2017, A&A, 607, A52

Andrillat Y., 1983, A&AS, 53, 319

Bonev T., et al., 2017, Bulgarian Astronomical Journal, 26, 67

Braes L. L. E., Miley G. K., 1972, Nature, 235, 273

Cao R., Liu F. K., Zhou Z. Q., Komossa S., Ho L. C., 2018, MNRAS, 480, 2929

Catanzaro G., 2013, A&A, 550, A79

Clark J. S., Tarasov A. E., Okazaki A. T., Roche P., Lyuty V. M., 2001, A&A, 380, 615

Cowley A. P., McLaughlin D. B., Toney J., MacConnell D. J., 1972, PASP, 84, 834

Dachs J., Hummel W., Hanuschik R. W., 1992, A&AS, 95, 437

Delgado-Martí H., Levine A. M., Pfahl E., Rappaport S. A., 2001, ApJ, 546, 455

Fabregat J., et al., 1992, A&A, 259, 522

Glebocki R., Sikorski J., Bielicz E., Krogulec M., 1986, A&A, 158, 392

Grundstrom E. D., et al., 2007, ApJ, 660, 1398

Hanuschik R. W., 1986, A&A, 166, 185

Hanuschik R. W., Kozok J. R., Kaiser D., 1988, A&A, 189, 147

Hanuschik R. W., Hummel W., Dietle O., Sutorius E., 1995, A&A, 300, 163

Hirata R., Kogure T., 1977, PASJ, 29, 477

Huang S.-S., 1972, ApJ, 171, 549

Kunjaya C., Hirata R., 1995, PASJ, 47, 589

Lee W.-K., Dempsey A. M., Lithwick Y., 2019, ApJ, 882, L11

Li H., Yan J., Zhou J., Liu Q., 2014, AJ, 148, 113

Lynch E. M., Ogilvie G. I., 2019, MNRAS, 488, 1127

Lyubimkov L. S., Rostopchin S. I., Roche P., Tarasov A. E., 1997, MNRAS, 286, 549

Martin R. G., Lissauer J. J., Quarles B., 2020, arXiv e-prints, p. arXiv:2006.05529

Matsuoka M., et al., 2009, PASJ, 61, 999

Nakajima M., Negoro H., Mihara T., Sugizaki M., Yatabe F., Makishima K., 2019, in Oskinova L. M., Bozzo E., Bulik T., Gies D. R., eds, IAU Symposium Vol. 346, IAU Symposium. pp 131–134

Negueruela I., 2007, in St. -Louis N., Moffat A. F. J., eds, Astronomical Society of the Pacific Conference Series Vol. 367, Massive Stars in Interactive Binaries. p. 477

Nemravová J., et al., 2010, A&A, 516, A80

Ogilvie G. I., 2008, MNRAS, 388, 1372

Okazaki A. T., 1991, PASJ, 43, 75

Okazaki A. T., 2016, in Sigut T. A. A., Jones C. E., eds, Astronomical Society of the Pacific Conference Series Vol. 506, Bright Emissaries: Be Stars as Messengers of Star-Disk Physics. p. 3

Okazaki A. T., Kato S., 1986, Ap&SS, 119, 109

Okazaki A. T., Bate M. R., Ogilvie G. I., Pringle J. E., 2002, MNRAS, 337, 967

Panoglou D., Faes D. M., Carciofi A. C., Okazaki A. T., Baade D., Rivinius T., Borges Fernandes M., 2018, MNRAS, 473, 3039

Papaloizou J. C. B., Savonije G. J., 2006, A&A, 456, 1097

Porter J. M., Rivinius T., 2003, PASP, 115, 1153

Reig P., 2011, Ap&SS, 332, 1

Rivinius T., Carciofi A. C., Martayan C., 2013, A&ARv, 21, 69

Roche P., et al., 1997, A&A, 322, 139

Savonije G. J., Heemskerk M. H. M., 1993, A&A, 276, 409

Schmitt J. H. M. M., et al., 2014, Astronomische Nachrichten, 335, 787

Slettebak A., 1982, ApJS, 50, 55

Slettebak A., Collins II G. W., Truax R., 1992, ApJS, 81, 335

Struve O., 1931, ApJ, 73, 94

Tarasov A. E., Roche P., 1995, MNRAS, 276, L19

Telting J. H., Waters L. B. F. M., Roche P., Boogert A. C. A., Clark J. S., de Martino D., Persi P., 1998, MNRAS, 296, 785

Yatabe F., Makishima K., Mihara T., Nakajima M., Sugizaki M., Kitamoto S., Yoshida Y., Takagi T., 2018, PASJ, 70, 89

Zamanov R., Stoyanov K. A., Wolter U., Marchev D., Petrov N. I., 2019, A&A, 622, A173

6 APPENDIX

This paper has been typeset from a TEX/LATEX file prepared by the author.

Table 2. Journal of observations. In the table are given date of observation, observatory, exposure time, Julian day (24400000+).

date-obs	Obs.	exp-time [sec]	JD
2015-12-23T23:16	Rozhen	1800	57380.47503
2015-12-23T23:48	Rozhen	600	57380.49672
2015-12-24T20:51	Rozhen	600	57381.37398
2015-12-26T20:01	Rozhen	600	57383.33892
2015-12-27T20:56	Rozhen	300	57384.37750
2016-01-30T19:10	Rozhen	300	57418.30099
2016-09-23T01:42	Rozhen	600	57654.57407
2016-09-23T01:42	Rozhen	600	57654.57407
2016-12-11T20:58	Rozhen	1200	57734.37953
2017-03-17T18:58	Rozhen	1200	57830.28854
2017-12-07T16:57	Rozhen	120	58095.21181
2017-12-07T17:03	Rozhen	900	58095.21620
2017-12-07T17:20	Rozhen	900	58095.22811
2017-12-08T16:45	Rozhen	120	58096.20389
2017-12-08T16:50	Rozhen	600	58096.20690
2017-12-21T03:34	"LaLuz"	240	58108.65399
2017-12-22T00:53	"LaLuz"	240	58109.54230
2017-12-23T00:54	"LaLuz"	127	58110.54298
2017-12-24T01:22	"LaLuz"	240	58111.56198
2017-12-25T01:26	"LaLuz"	242	58112.56500
2017-12-30T19:20	Rozhen	1200	58118.31067
2018-01-01T17:23	Rozhen	1200	58120.22886
2018-01-04T01:28	"LaLuz"	900	58122.56566
2018-01-04T03:56	"LaLuz"	900	58122.66813
2018-01-04T06:17	"LaLuz"	900	58122.76651
2018-01-05T01:21	"LaLuz"	900	58123.56049
2018-01-06T01:59	"LaLuz"	900	58124.58737
2018-01-06T04:19	"LaLuz"	900	58124.68461
2018-01-06T06:39	"LaLuz"	300	58124.78160
2018-01-07T01:23	"LaLuz"	900	58125.56225
2018-01-07T03:49	"LaLuz"	900	58125.66353
2018-01-07T06:14	"LaLuz"	900	58125.76423
2018-01-26T17:09	Rozhen	120	58145.21745
2018-01-26T17:12	Rozhen	180	58145.21951
2018-01-26T17:16	Rozhen	900	58145.22261
2018-01-26T17:32	Rozhen	1200	58145.23371
2018-02-01T17:09	Rozhen	1200	58151.21687
2018-02-01T17:30	Rozhen	300	58151.23149
2018-04-02T18:42	Rozhen	600	58211.27615
2018-04-02T18:53	Rozhen	120	58211.28358
2018-07-20T11:09	"LaLuz"	600	58319.96179
2018-08-02T11:20	"LaLuz"	600	58332.97006
2018-08-18T10:06	"LaLuz"	600	58348.92028
2018-08-19T01:10	Rozhen	120	58349.54794
2018-08-19T01:14	Rozhen	900	58349.55114
2018-08-30T00:11	Rozhen	600	58360.50863
2018-08-30T00:23	Rozhen	120	58360.51631
2018-08-31T01:50	Rozhen	600	58361.57747
2018-08-31T02:01	Rozhen	120	58361.58508
2018-09-01T01:13	Rozhen	600	58362.55181
2018-09-01T01:25	Rozhen	120	58362.55977
2018-09-02T02:39	Rozhen	600	58363.61129
2018-09-02T02:50	Rozhen	120	58363.61871
2018-09-03T01:21	Rozhen	600	58364.55719
2018-09-03T01:31	Rozhen	120	58364.56449
2018-09-05T08:54	"LaLuz"	600	58366.87215
2018-09-25T08:49	"LaLuz"	600	58386.87070
2018-10-10T07:16	"LaLuz"	600	58401.80672
2018-11-24T06:04	"LaLuz"	600	58446.75842
2018-11-25T22:30	Rozhen	180	58448.44317
2018-12-06T07:11	"LaLuz"	900	58458.80544
2018-12-18T07:07	"LaLuz"	900	58470.80209
2018-12-20T20:54	Rozhen	120	58473.37615
2018-12-20T20:57	Rozhen	900	58473.37847

Table 2. Journal of observations (continuation).

2018-12-21T18:18	Rozhen	120	58474.26792
2018-12-21T18:21	Rozhen	900	58474.26989
2018-12-27T22:31	Rozhen	600	58480.44336
2018-12-27T22:42	Rozhen	120	58480.45117
2018-12-30T07:12	"LaLuz"	900	58482.80473
2019-01-11T07:14	"LaLuz"	900	58494.80544
2019-01-18T20:16	Rozhen	60	58502.34774
2019-01-18T20:19	Rozhen	120	58502.34988
2019-01-18T20:23	Rozhen	720	58502.35273
2019-01-18T20:37	Rozhen	900	58502.36252
2019-01-24T01:12	"LaLuz"	900	58507.55335
2019-02-07T01:37	"LaLuz"	900	58521.56939
2019-02-20T16:41	Rozhen	900	58535.19549
2019-02-20T16:57	Rozhen	120	58535.20681
2019-02-21T17:38	Rozhen	1200	58536.23481
2019-02-21T17:58	Rozhen	120	58536.24923
2019-03-02T01:51	"LaLuz"	1125	58544.57689
2019-03-17T18:50	Rozhen	600	58560.28307
2019-03-17T19:02	Rozhen	120	58560.29132
2019-03-23T19:10	Rozhen	120	58566.29626
2019-03-23T19:14	Rozhen	900	58566.29891
2019-03-25T18:19	Rozhen	120	58568.26056
2019-03-25T18:22	Rozhen	900	58568.26288
2019-07-18T00:30	Rozhen	600	58682.51763
2019-07-18T00:41	Rozhen	120	58682.52516
2019-07-19T00:51	Rozhen	600	58683.53222
2019-07-19T01:01	Rozhen	120	58683.53957
2019-08-19T00:43	Rozhen	600	58714.52967
2019-08-19T00:54	Rozhen	1200	58714.53737
2019-08-22T23:06	Rozhen	600	58718.46281
2019-08-22T23:18	Rozhen	120	58718.47082
2019-09-15T00:36	Rozhen	900	58741.52743
2019-09-15T00:53	Rozhen	120	58741.53915
2019-11-15T22:43	Rozhen	900	58803.45246
2019-11-15T22:43	Rozhen	900	58803.45246
2019-12-05T20:30	Rozhen	600	58823.35991
2019-12-05T20:41	Rozhen	120	58823.36759
2019-12-06T19:02	Rozhen	600	58824.29886
2019-12-06T19:13	Rozhen	120	58824.30628
2020-01-03T17:55	Rozhen	600	58852.25124
2020-01-03T18:06	Rozhen	120	58852.25892
2020-01-07T16:51	Rozhen	1200	58856.20631
2020-01-07T17:12	Rozhen	3600	58856.22133
2020-01-10T17:17	Rozhen	120	58859.22428
2020-01-10T17:23	Rozhen	900	58859.22862
2020-01-16T19:51	Rozhen	900	58865.33101
2020-01-16T20:08	Rozhen	120	58865.34259

Table 3. Parameters of the $H\alpha$ emission line. In the table are given Julian day (2400000+), equivalent width, intensity of the violet and red peaks, distance between the peaks, radial velocities of the peaks.

JD	$W\alpha$	I_B	I_R	ΔV [km s^{-1}]	V [km s^{-1}]	V [km s^{-1}]
58095.21084	-24.96	5.530	5.547	119.8	-72.3	48.2
58095.21523	-24.09	5.316	5.252	121.0	-72.9	48.0
58095.22714	-23.61	5.365	5.316	119.7	-72.7	47.7
58096.20296	-24.43	5.581	5.598	119.0	-72.7	47.6
58096.20597	-24.22	5.521	5.422	121.6	-73.3	49.3
58118.31064	-22.61	4.954	5.006	123.7	-77.5	45.9
58120.22892	-20.32	4.839	4.875	120.8	-76.0	44.0
58145.21851	-18.61	4.162	4.709	108.0	-74.5	33.5
58145.22057	-18.67	4.146	4.755	108.4	-77.0	33.9
58145.22368	-18.25	4.141	4.741	110.3	-76.5	33.7
58145.23478	-18.55	4.146	4.619	109.6	-76.2	33.1
58151.21816	-18.77	4.076	4.859	116.2	-85.1	32.5
58151.23277	-17.68	4.068	4.881	116.1	-82.5	32.3
58211.27855	-16.35	3.519	4.480	106.6	-89.0	17.6
58211.28598	-15.92	3.628	4.511	102.4	-86.8	17.9
58349.54619	-18.81	3.440	5.197	105.3	-98.0	12.4
58349.54938	-17.66	3.409	5.159	98.0	-98.7	10.3
58360.50660	-18.42	3.278	5.383	100.7	-93.8	9.2
58360.51428	-18.84	3.309	5.345	105.8	-96.8	10.8
58361.57541	-17.77	3.139	5.173	97.8	-90.0	3.2
58361.58303	-18.42	3.158	5.258	87.9	-89.5	2.9
58362.54974	-18.92	3.247	5.363	94.8	-89.0	5.3
58362.55770	-18.49	3.245	5.343	100.8	-92.8	3.9
58363.60919	-19.45	3.292	5.438	98.5	-94.8	1.5
58363.61661	-18.86	3.284	5.417	95.2	-93.8	2.5
58364.55507	-18.88	3.304	5.386	95.2	-96.9	2.9
58364.56238	-19.03	3.293	5.419	99.9	-93.5	0.8
58448.44176	-21.17	3.371	5.767	115.9	-115.0	2.1
58473.37570	-19.99	3.663	5.509	108.2	-103.3	7.7
58473.37802	-20.87	3.607	5.397	115.2	-106.1	6.3
58474.26750	-20.30	3.606	5.448	110.6	-101.9	9.2
58474.26947	-20.24	3.507	5.400	112.9	-105.6	5.8
58480.44321	-21.40	3.710	5.538	112.0	-106.1	8.1
58480.45101	-21.28	3.802	5.691	110.4	-106.5	8.8
58502.34850	-20.51	3.822	5.251	105.8	-99.7	11.6
58502.35064	-20.05	3.836	5.252	109.7	-104.7	12.1
58502.35348	-20.54	3.809	5.196	109.3	-103.1	12.0
58502.36328	-20.25	3.833	5.222	112.0	-102.5	11.7
58535.19736	-19.42	3.714	5.307	114.6	-94.8	21.8
58535.20868	-20.20	3.747	5.353	115.9	-94.4	20.4
58536.23671	-20.01	3.678	5.219	116.5	-97.8	21.7
58536.25113	-19.68	3.743	5.286	117.6	-98.7	20.8
58560.28540	-20.20	3.905	4.708	108.3	-87.3	21.9
58560.29365	-19.43	3.893	4.837	106.9	-85.9	21.0
58566.29864	-21.40	4.367	4.845	108.3	-87.6	26.7
58566.30129	-20.18	4.117	4.788	110.6	-86.3	25.8
58568.26295	-19.94	4.175	4.693	107.3	-82.3	25.3
58568.26527	-20.45	4.093	4.686	108.3	-81.8	25.4
58108.65545	-23.37	5.518	5.257	125.3	-69.8	56.3
58109.54377	-23.51	5.421	5.273	121.6	-66.1	58.4
58110.54374	-24.88	5.477	5.217	123.8	-69.0	55.1
58111.56345	-26.02	5.385	5.244	125.2	-72.0	50.6
58112.56647	-23.20	5.046	5.056	123.9	-65.5	57.3
58122.57100	-20.95	4.840	4.850	124.3	-72.3	51.6
58122.67347	-21.42	4.890	4.931	123.4	-73.8	50.4
58122.77185	-21.03	4.859	4.884	124.6	-74.0	50.4
58123.56582	-22.24	5.003	5.008	125.2	-72.7	51.3

Table 3. continuation.

58124.59271	-22.08	4.983	4.921	122.4	-74.1	49.0
58124.68994	-20.87	4.933	4.892	122.4	-74.8	47.8
58124.78338	-20.99	4.921	4.856	122.6	-75.1	48.5
58125.56759	-20.60	4.849	4.829	123.2	-72.0	50.9
58125.66887	-20.71	4.888	4.872	122.0	-72.9	49.2
58125.76956	-21.29	4.902	4.887	122.2	-73.7	49.6
58319.96541	-16.63	3.143	4.770	107.5	-95.4	18.2
58332.97367	-16.86	3.144	5.053	107.9	-96.7	16.2
58348.92388	-19.44	3.499	5.272	100.4	-96.5	12.7
58366.87575	-20.47	3.436	5.451	100.3	-93.3	12.4
58386.87432	-20.88	3.508	5.680	98.9	-102.3	6.1
58401.81034	-21.58	3.908	5.515	100.3	-96.5	8.1
58446.76209	-20.95	3.400	5.717	120.5	-112.6	8.3
58458.81081	-19.76	3.172	5.571	117.9	-116.1	12.3
58470.80746	-20.75	3.496	5.368	114.9	-108.5	13.3
58482.81011	-20.85	3.744	5.403	105.9	-99.0	10.7
58494.81083	-21.35	3.815	5.372	90.4	-85.8	10.6
58507.55874	-20.20	3.730	5.266	102.4	-95.2	16.5
58521.57478	-20.01	3.636	5.246	116.7	-98.1	20.6
58544.58365	-20.18	3.939	5.038	109.6	-84.3	31.4
58682.52460	-16.63	4.196	3.755	110.5	-82.3	26.0
58682.52940	-17.08	—	—	—	—	—
58683.53920	-17.11	4.182	3.864	112.7	-83.0	24.2
58683.54370	-16.64	4.261	3.931	109.1	-73.7	21.7
58714.53390	-15.77	3.998	3.579	103.3	-75.1	25.5
58714.54510	-15.39	4.002	3.633	108.1	-75.1	28.5
58718.46660	-15.81	3.925	3.686	110.3	-75.6	34.2
58718.47190	-15.64	3.951	3.740	110.3	-76.4	36.0
58741.53080	-14.26	4.135	3.377	106.1	-68.5	34.3
58741.53800	-14.31	4.158	3.432	102.1	-67.5	28.7
58803.45210	-12.39	3.829	2.898	112.9	-55.4	57.2
58803.45210	-12.49	3.835	2.916	111.1	-55.7	56.4
58823.35790	-11.58	3.637	2.550	107.7	-50.6	59.7
58823.36280	-11.03	3.625	2.548	110.5	-49.6	63.9
58824.29680	-11.66	3.621	2.482	109.1	-55.1	58.6
58824.30150	-10.92	3.618	2.481	113.3	-55.8	59.7
58852.25040	-10.15	3.294	2.374	119.2	-58.2	56.4
58852.25530	-10.26	3.339	2.398	114.4	-58.1	58.1
58856.20920	-10.51	3.251	2.395	106.8	-56.3	54.8
58856.23810	-10.32	3.179	2.347	110.5	-58.6	55.1
58859.22110	-10.33	3.176	2.372	125.3	-58.7	67.4
58859.23000	-10.06	3.153	2.362	127.7	-58.8	65.6
58865.33290	-10.20	3.161	2.370	120.8	-59.7	63.1
58865.33990	-10.19	3.231	2.414	119.4	-60.4	62.9

Table 4. Parameters of the $H\beta$ emission line. In the table are given Julian day (2400000+), equivalent width, intensity of the violet and red peaks, distance between the peaks.

58095.21084	-4.357	2.094	2.167	150.5	-87.3	61.7	—
58095.21523	-4.140	2.092	2.115	150.9	-86.5	64.2	—
58095.22714	-4.172	2.088	2.116	151.0	-87.3	63.9	—
58096.20296	-4.132	2.161	2.131	148.9	-85.8	63.3	—
58096.20597	-4.184	2.122	2.115	148.8	-88.1	61.7	—
58118.31064	-3.699	1.965	2.094	148.1	-91.9	58.7	—
58120.22892	-3.814	1.944	2.106	143.9	-87.9	56.7	—
58145.21851	-3.262	1.775	2.039	141.5	-78.7	65.7	—
58145.22057	-3.315	1.763	2.048	137.0	-78.1	62.8	—
58145.22368	-3.322	1.754	2.015	140.1	-78.9	63.3	—
58145.23478	-3.360	1.762	2.023	140.3	-80.2	62.5	—
58151.21816	-3.259	1.725	2.074	138.0	-102.0	40.0	—
58151.23277	-3.509	1.747	2.088	141.8	-107.1	40.0	—
58211.27855	-2.544	1.548	1.918	106.5	-84.4	28.8	—
58211.28598	-2.683	1.545	1.936	127.6	-97.2	28.0	—
58349.54619	-3.123	1.520	2.095	125.0	-119.1	19.3	—
58349.54938	-3.150	1.505	2.018	130.0	-113.1	21.7	—
58360.50660	-2.963	1.449	2.035	132.7	-120.0	19.6	—
58360.51428	-3.062	1.469	2.059	131.5	-115.7	18.7	—
58361.57541	-3.034	1.413	2.021	131.2	-116.9	19.6	—
58361.58303	-3.096	1.437	2.040	135.7	-111.8	20.4	—
58362.54974	-2.815	1.439	2.072	137.4	-116.8	17.9	—
58362.55770	-3.151	1.447	2.062	139.1	-124.8	19.3	—
58363.60919	-3.133	1.434	2.066	140.0	-121.7	18.4	—
58363.61661	-2.993	1.437	2.068	130.8	-117.9	16.0	—
58364.55507	-3.103	1.460	2.038	141.3	-155.3	-18.6	—
58364.56238	-3.072	1.475	2.023	144.1	-153.9	-16.1	—
58448.44176	-3.263	1.552	2.021	163.8	-155.9	10.1	—
58473.37570	-3.328	1.576	2.012	147.7	-122.6	25.2	—
58473.37802	-3.450	1.548	1.985	147.8	-123.4	22.2	—
58474.26750	-3.288	1.535	2.106	158.2	-130.1	25.0	—
58474.26947	-3.219	1.515	2.010	148.9	-124.8	23.5	—
58480.44321	-3.179	1.549	2.005	153.6	-127.9	21.5	—
58480.45101	-3.078	1.549	2.026	148.9	-126.9	20.6	—
58502.34850	-3.392	1.597	1.933	145.1	-99.0	40.1	—
58502.35064	-3.229	1.590	1.910	150.2	-107.6	39.4	—
58502.35348	-3.347	1.601	1.932	149.4	-108.9	41.1	—
58502.36328	-3.307	1.588	1.923	152.4	-109.7	40.1	—
58535.19736	-3.198	1.569	1.866	150.0	-122.2	27.5	—
58535.20868	-3.131	1.590	1.941	152.8	-125.8	26.1	—
58536.23671	-2.858	1.574	1.875	158.9	-128.8	29.1	—
58536.25113	-2.988	1.601	1.897	161.1	-127.4	29.4	—
58560.28540	-2.870	1.629	1.726	147.6	-118.7	29.5	—
58560.29365	-2.885	1.661	1.739	145.0	-118.6	27.7	—
58566.29864	-3.198	1.772	1.809	146.9	-117.2	28.4	—
58566.30129	-2.738	1.672	1.691	—	—	—	—
58568.26295	-2.934	1.706	1.732	148.7	-115.8	25.1	—
58568.26527	-3.073	1.698	1.707	146.0	-115.5	30.4	—
58108.65545	-4.003	1.969	2.157	152.7	-84.4	68.1	—
58109.54377	-3.924	1.971	2.126	145.7	-83.1	62.5	—
58110.54374	-4.017	2.109	2.273	145.2	—	—	—
58111.56345	-4.062	1.999	2.206	149.0	-88.7	63.9	—
58112.56647	-3.892	2.006	2.168	147.0	-84.4	63.1	—
58122.57100	-3.621	1.835	2.059	148.4	-94.9	58.0	—
58122.67347	-3.521	1.892	2.053	149.8	-91.5	56.0	—
58122.77185	-3.525	1.845	2.039	150.0	-94.5	57.7	—
58123.56582	-3.613	1.880	2.062	148.7	-90.5	57.6	—
58124.59271	-3.615	1.899	2.066	146.3	-87.6	58.1	—
58124.68994	-3.488	1.868	2.023	145.8	-89.9	54.9	—
58124.78338	-3.548	1.855	2.047	143.8	-86.6	55.0	—

Table 4. continuation.

58125.56759	-3.582	1.871	2.059	140.7	-89.7	53.3	—
58125.66887	-3.569	1.917	2.035	142.8	-89.2	54.6	—
58125.76956	-3.541	1.859	2.021	143.0	-88.7	55.5	—
58319.96541	-2.779	1.442	1.966	120.2	-97.5	26.2	—
58332.97367	-2.733	1.450	1.980	126.0	—	—	—
58348.92388	-2.979	1.536	2.031	127.2	-106.0	21.4	—
58366.87575	-3.002	1.505	2.076	124.7	-106.5	18.9	—
58386.87432	-3.309	1.474	2.056	144.2	-130.4	18.4	—
58401.81034	-3.424	1.598	2.047	139.0	-124.3	17.0	—
58446.76209	-3.257	1.578	2.034	166.9	-152.5	16.2	—
58458.81081	-3.001	1.509	2.006	167.5	-147.9	20.1	—
58470.80746	-3.126	1.541	1.964	152.3	-128.5	23.2	—
58482.81011	-3.067	1.556	1.911	141.6	-121.9	21.7	—
58494.81083	-3.104	1.523	1.956	146.7	-126.4	21.1	—
58507.55874	-3.032	1.565	1.852	156.7	-127.8	27.3	—
58521.57478	-2.855	1.567	1.842	157.9	-132.4	27.8	—
58544.58365	-2.764	1.584	1.773	155.7	-114.4	38.8	—
58682.52460	-2.246	1.630	1.400	117.1	-98.3	23.3	220.0
58682.52940	—	—-	—	—	—	—	—
58683.53920	-2.309	1.598	1.377	113.2	-100.5	23.8	206.6
58683.54370	-2.355	1.604	1.400	109.8	-100.4	17.1	196.9
58714.53390	-2.100	1.619	1.357	123.3	-90.8	24.9	202.2
58714.54510	-2.015	1.603	1.358	119.9	-91.5	31.5	197.5
58718.46660	-2.039	1.608	1.389	122.0	-89.8	34.2	197.7
58718.47190	-2.009	1.598	1.433	122.2	-89.7	31.0	191.5
58741.53080	-1.896	1.615	1.315	125.3	-81.0	47.2	207.0
58741.53800	-2.019	1.661	1.324	141.8	-81.2	24.8	194.1
58803.45210	-1.675	1.536	1.261	131.4	-70.8	65.4	170.1
58803.46410	-1.594	1.518	1.248	130.0	-70.2	61.8	163.1
58823.35790	-1.571	1.502	1.215	128.1	-65.7	65.9	162.5
58823.36280	-1.628	1.509	1.251	126.2	-65.4	63.7	166.7
58824.29680	-1.456	1.497	1.202	128.7	-68.7	65.2	153.4
58824.30150	-1.507	1.479	1.224	127.3	-68.8	60.1	151.3
58852.25040	-1.438	1.439	1.119	149.0	-68.7	89.0	—
58852.25530	-1.473	1.467	1.225	148.9	-69.1	96.8	—
58856.20920	-1.498	1.415	1.242	155.8	-67.9	88.3	—
58856.23810	-1.481	1.429	1.221	147.2	-68.4	86.5	—
58859.22110	-1.475	1.422	1.224	152.3	-68.7	89.3	—
58859.23000	-1.427	1.421	1.210	148.7	-68.6	78.7	—
58865.33290	-1.427	1.434	1.244	173.3	-67.6	96.1	—
58865.33990	-1.366	1.431	1.259	165.5	-69.4	87.3	—

Table 5. Parameters of the HeI 6678 emission line. In the table are given Julian day (2400000+), equivalent width, intensity of the violet and red peaks, distance between the peaks, radial velocities of the peaks.

JD	$W\alpha$	I_B	I_R	ΔV [km s^{-1}]	V [km s^{-1}]	V [km s^{-1}]	V [km s^{-1}]
58095.21084	-2.004	1.363	1.346	181.9	-98.0	81.7	
58095.21523	-1.908	1.334	1.323	182.5	-95.5	84.2	
58095.22714	-1.917	1.327	1.325	178.9	-100.2	82.7	
58096.20296	-2.030	1.344	1.363	178.3	-101.0	81.0	
58096.20597	-1.973	1.340	1.330	179.3	-98.3	84.8	
58118.31064	-1.564	1.278	1.301	180.9	-111.3	71.2	
58120.22892	-1.470	1.264	1.272	169.3	-102.8	67.8	
58145.21851	-1.118	1.185	1.240	159.1	-105.6	52.8	
58145.22057	-1.229	1.179	1.251	154.6	-99.8	53.6	
58145.22368	-1.193	1.174	1.246	155.1	-106.6	53.1	
58145.23478	-1.202	1.183	1.242	164.2	-111.5	54.2	
58151.21816	-1.180	1.178	1.263	165.3	-116.1	49.5	
58151.23277	-1.073	1.193	1.271	168.0	-115.8	52.8	
58211.27855	-0.865	1.107	1.206	166.8	-127.2	43.1	
58211.28598	-0.922	1.114	1.209	—	—	—	
58349.54619	-0.904	1.110	1.210	201.8	-164.5	34.3	
58349.54938	-0.816	1.100	1.195	202.8	-169.8	35.3	
58360.50660	-0.932	1.109	1.196	212.0	-181.8	29.9	
58360.51428	-0.907	1.113	1.209	190.3	-165.4	26.0	
58361.57541	-0.939	1.109	1.212	211.7	-185.9	29.1	
58361.58303	-0.911	1.106	1.218	200.5	-173.1	28.8	
58362.54974	-0.927	1.095	1.214	201.2	-167.9	30.2	
58362.55770	-0.950	1.103	1.205	196.0	-161.1	31.5	
58363.60919	-1.044	1.099	1.219	209.0	-179.9	29.8	
58363.61661	-1.089	1.107	1.231	204.9	-172.4	29.9	
58364.55507	-1.112	1.107	1.200	209.7	-173.5	28.8	
58364.56238	-1.104	1.121	1.205	201.8	-172.6	30.6	
58448.44176	-1.586	1.197	1.243	206.9	-182.7	25.4	
58473.37570	-1.749	1.201	1.244	217.6	-189.1	32.5	
58473.37802	-1.665	1.178	1.210	211.5	-188.1	27.2	199.1
58474.26750	-1.540	1.218	1.262	212.2	-185.4	25.3	—
58474.26947	-1.573	1.186	1.212	218.3	-190.9	26.5	187.0
58480.44321	-1.653	1.214	1.227	218.8	-190.9	28.0	163.3
58480.45101	-1.942	1.265	1.297	205.2	-185.5	26.1	—
58502.34850	-1.550	1.233	1.216	199.9	-176.6	22.1	—
58502.35064	-1.580	1.208	1.194	201.7	-171.3	28.6	—
58502.35348	-1.475	1.212	1.197	198.4	-166.7	28.0	205.8
58502.36328	-1.591	1.211	1.193	201.7	-172.5	27.5	206.8
58535.19736	-1.505	1.205	1.178	191.2	-157.2	32.2	231.0
58535.20868	-1.536	1.217	1.195	192.6	-162.1	34.6	204.6
58536.23671	-1.505	1.205	1.171	180.2	-149.2	34.5	229.0
58536.25113	-1.522	1.221	1.183	185.4	-152.7	31.8	234.8
58560.28540	-1.427	1.216	1.138	177.4	-144.8	30.0	246.5
58560.29365	-1.520	1.232	1.130	176.2	-152.9	28.7	223.3
58566.29864	-1.648	1.242	1.175	-1.0	—	—	—
58566.30129	-1.470	1.220	1.141	160.2	-144.8	23.5	245.2
58568.26295	-1.486	1.229	1.159	141.9	-138.9	11.1	250.1
58568.26527	-1.375	1.224	1.142	162.2	-133.3	25.5	240.9
58108.65545	-1.501	1.233	1.312	180.5	-94.5	84.2	
58109.54377	-1.485	1.240	1.314	177.0	-87.3	87.2	
58110.54374	-1.417	1.246	1.316	174.6	-90.6	80.2	
58111.56345	-1.406	1.214	1.315	174.1	-92.9	80.1	
58112.56647	-1.417	1.247	1.332	181.2	-94.4	85.8	
58122.57100	-1.180	1.199	1.292	181.0	-105.4	75.1	
58122.67347	-1.165	1.197	1.280	183.2	-107.5	73.5	
58122.77185	-1.120	1.198	1.280	184.3	-105.2	75.2	
58123.56582	-1.129	1.199	1.276	178.9	-100.1	76.1	

Table 5. continuation.

58124.59271	-1.115	1.198	1.265	173.3	-98.1	74.1	
58124.68994	-1.113	1.197	1.273	170.8	-98.3	73.4	
58124.78338	-1.134	1.200	1.281	172.2	-97.6	71.7	
58125.56759	-1.114	1.190	1.277	173.0	-97.2	74.3	
58125.66887	-1.176	1.190	1.281	175.5	-97.3	73.8	
58125.76956	-1.124	1.191	1.268	178.0	-99.8	73.1	
58319.96541	-0.687	1.074	1.149	209.9	-156.8	35.3	
58332.97367	-0.707	1.078	1.171	219.8	-182.9	37.3	
58348.92388	-0.857	1.105	1.186	210.5	-178.2	32.3	
58366.87575	-0.936	1.108	1.197	203.8	-176.2	35.9	
58386.87432	-1.162	1.141	1.198	233.5	-204.5	35.7	
58401.81034	-1.269	1.166	1.210	215.9	-184.4	36.9	
58446.76209	-1.383	1.207	1.197	217.8	-183.2	32.8	
58458.81081	-1.319	1.159	1.193	223.6	-192.5	32.1	
58470.80746	-1.326	1.170	1.196	223.3	-185.8	35.0	
58482.81011	-1.475	1.196	1.204	211.6	-179.6	30.0	201.7
58494.81083	-1.394	1.187	1.202	201.5	-177.1	24.7	174.4
58507.55874	-1.454	1.218	1.171	206.1	-174.9	33.9	208.6
58521.57478	-1.381	1.188	1.167	196.6	-167.8	28.4	217.5
58544.58365	-1.351	1.206	1.167	179.0	-142.5	36.9	232.3
58682.52460	-0.896	1.223	1.089	367.4	-117.1	242.3	
58683.53920	-0.873	1.229	1.081	357.9	-120.7	235.8	
58683.54370	-0.817	1.228	1.106	358.4	-116.9	244.8	
58714.53390	-0.813	1.180	1.088	348.2	-104.4	242.5	
58714.54510	-0.781	1.176	1.083	353.4	-107.6	244.7	
58718.46660	-0.796	1.182	1.081	345.4	-104.5	239.8	
58718.47190	-0.808	1.192	1.104	341.3	-103.1	240.1	
58741.53080	-0.716	1.197	1.081	331.9	-95.1	240.6	
58741.53800	-0.727	1.191	1.091	335.8	-92.9	235.8	
58803.45210	-0.586	1.129	1.092	279.2	-72.6	208.5	
58803.46410	-0.570	1.120	1.091	271.5	-72.6	201.9	
58823.35790	-0.510	1.115	1.080	257.3	-67.3	195.5	
58823.36280	-0.518	1.122	1.091	260.1	-67.6	197.3	
58824.29680	-0.521	1.118	1.092	263.3	-73.2	192.4	
58824.30150	-0.494	1.121	1.094	267.6	-74.4	192.9	
58852.25040	-0.436	1.110	1.069	244.1	-67.8	179.2	
58852.25530	-0.446	1.118	1.079	254.5	-68.4	179.4	
58856.20920	-0.422	1.107	1.081	225.4	-67.6	160.1	
58856.23810	-0.413	1.088	1.087	231.4	-67.2	163.2	
58859.22110	-0.401	—	—	—	—	—	
58859.23000	-0.417	1.098	1.073	223.4	-70.8	152.7	
58865.33290	-0.417	1.086	1.078	216.4	-64.9	150.5	